

Nonlinear detection of spin currents in graphene with non-magnetic electrodes

Ivan J. Vera-Marun^{*}, Vishal Ranjan and Bart J. van Wees

The abilities to inject and detect spin carriers are fundamental for research on transport and manipulation of spin information^{1,2}. Pure electronic spin currents have been recently studied in nanoscale electronic devices using a non-local lateral geometry, both in metallic systems³ and in semiconductors⁴. To unlock the full potential of spintronics we must understand the interactions of spin with other degrees of freedom. Such interactions have been explored recently, for example, by using spin Hall^{5–7} or spin thermoelectric effects^{6,8,9}. Here we present the detection of non-local spin signals using non-magnetic detectors, through an as-yet-unexplored nonlinear interaction between spin and charge. In analogy to the Seebeck effect¹⁰, where a heat current generates a charge potential, we demonstrate that a spin current in a paramagnet leads to a charge potential, if the conductivity is energy dependent. We use graphene¹¹ as a model system to study this effect, as recently proposed¹². The physical concept demonstrated here is generally valid, opening new possibilities for spintronics.

Previous reports on detection of spin signals using non-magnetic contacts have made use of spin–orbit interaction through the (inverse) spin Hall effect^{5,6}. Recently, large non-local signals in graphene have been attributed to an effect with similar phenomenology, given by the difference in Hall resistance between two (spin) channels induced by an applied perpendicular magnetic field⁷. Both effects produce a charge potential transversal to the direction of the spin current and are valid in the linear regime. In the present work we deal with a different concept based on a nonlinear interaction between spin and charge which results in charge potentials longitudinal to the spin current¹². This effect is solely based on the energy dependence of the conductivity $\sigma(\epsilon)$, not requiring spin–orbit interaction or external magnetic fields.

To explain the concept of detection of spin signals used here it is useful to make an analogy with thermoelectrics. As shown in Fig. 1a, a temperature gradient sets up a heat current. Under open-circuit conditions, this results in a built-up voltage $V = -S(T_2 - T_1)$, with S the Seebeck coefficient of the conducting system. For the case of diffusive spin transport¹³ (Fig. 1b) the electrochemical potential of each spin channel can be described as $\mu_{\pm} = \mu_{\text{avg}} \pm \Delta\mu$, with $\Delta\mu$ the spin accumulation (created by electrical spin injection) in the conductor, which decays with a characteristic spin-relaxation length λ . The gradient in spin accumulation sets up a spin current, which results, for ferromagnetic or ferrimagnetic materials with a spin polarization of the conductivity¹³ β , in a built-up voltage $V = -(\beta/e)(\Delta\mu_2 - \Delta\mu_1)$. While S is a general property of conductors, β is in general zero for paramagnetic materials. Therefore, pure spin currents are not expected to generate charge voltages in a paramagnet such as graphene. The latter is not true if we consider spin transport away from the Fermi level. When a sizable $\Delta\mu$ is present, each spin channel experiences a different

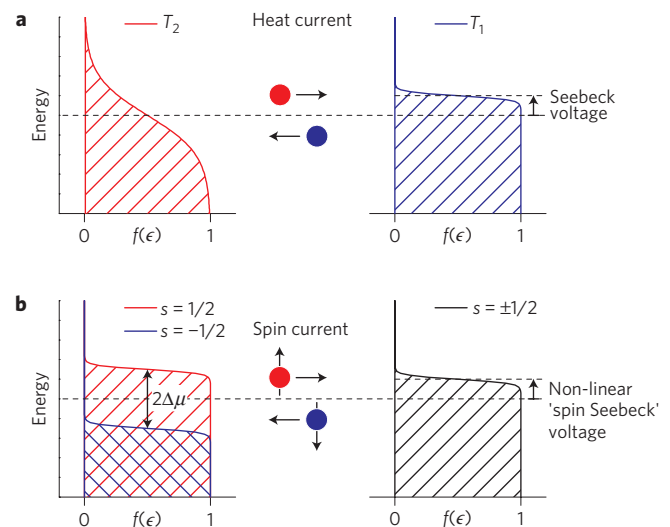


Figure 1 | Analogy between spin and heat transport illustrated by electronic distributions $f(\epsilon)$. **a**, A temperature gradient ($T_2 > T_1$) sets up a heat current, with high-energy electrons moving towards the cold region and low-energy electrons moving towards the hot region. When the conductivity is energy dependent (here $\partial\sigma/\partial\epsilon > 0$) a Seebeck voltage is built up under open-circuit conditions, to compensate for the different conductivities of high- and low-energy electrons. **b**, A gradient in spin accumulation $\Delta\mu$ sets up a spin current, with majority-spin electrons moving towards the region with lower $\Delta\mu$ and minority-spin electrons moving in the opposite direction. Similar to thermoelectricity, a voltage is built up if the conductivity is energy dependent owing to the different conductivities of the two electron spin species.

conductivity even in a paramagnet, as long as the conductivity is energy dependent. So we consider a spin polarization of the conductivity induced by $\Delta\mu$, which can be approximated as¹² $\beta = -\Delta\mu\sigma^{-1}\partial\sigma/\partial\epsilon$.

To complete the analogy, we define $\alpha = \sigma^{-1}\partial\sigma/\partial\epsilon$. The previous expressions for V are only valid when the coefficients S and β are independent of the driving forces T and $\Delta\mu$, respectively. In reality, the Seebeck coefficient is given by the Mott formula^{10,14} $S = -L_0\alpha T$, with $L_0 = (\pi^2/3)(k_B^2/e^2)$ the Lorentz number. In the limit $T \approx T_2 - T_1$, the Seebeck voltage depends quadratically on the driving force as $V \propto L_0\alpha\epsilon(T)^2$. Similarly, for spin transport in a paramagnet, the induced spin polarization mentioned above ($\beta = -\alpha\Delta\mu$) also results in a quadratic dependence on the driving force as $V \propto (\alpha/e)(\Delta\mu)^2$. Owing to the common factor α the effect described here has similar behaviour to the Seebeck voltage, showing opposite polarity for electron and hole regimes.

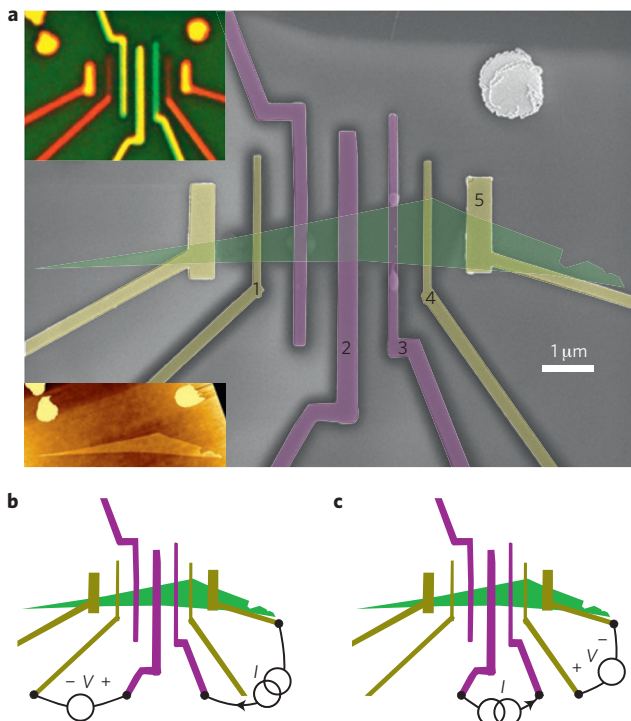


Figure 2 | Sample geometry and non-local measurement configuration.

a, Coloured scanning electron microscopy image of the device (after measurement and sample failure). Tunnel contacts have electrodes made of 5/25-nm-thick Ti/Au (contacts 1, 4 and 5) or 30-nm-thick Co (contacts 2 and 3). Upper inset: Optical image before measurement. Lower inset: Atomic force microscopy image of graphene before contact deposition. **b**, Configuration for measuring linear spin resistance using a magnetic detector. **c**, Configuration for measuring nonlinear resistance using non-magnetic detectors.

Furthermore, because $\Delta\mu$ is (to lowest order) linear in the injection current^{3,15}, the result is a second-order signal $V \propto I^2$.

For our proof of concept we use graphene, which, apart from being a two-dimensional platform for relativistic quantum mechanics¹¹, has proved to be an excellent system for spin transport, where large values of $\Delta\mu \approx 1$ meV can be obtained¹⁵. The sample is shown in Fig. 2a. It consists of a lateral graphene field-effect transistor covered with a thin aluminium oxide barrier that yields high-resistance contacts for efficient spin transport¹⁶ and electrostatic gating through the Si/SiO₂ substrate, as previously reported^{15,17}. As well as using magnetic Co contacts for electrical spin injection and detection (Fig. 2b), we also include Ti/Au contacts. These non-magnetic contacts are used to electrically detect spins in the configuration shown in Fig. 2c. There are two key aspects to such a measurement configuration. First, the use of non-magnetic detectors simplifies the analysis of the non-local signal, because for the case of using magnetic detectors both linear and nonlinear signals are expected owing to direct detection of $\Delta\mu$ (refs 12,18). Second, the use of two magnetic contacts as source and drain for charge current enables us to measure the non-local signal for both parallel V^{Pa} and antiparallel V^{Ap} alignment of their magnetizations and thereby to focus on the difference between the two states ΔV . This way we can exclude background signals that do not depend on $\Delta\mu$ and can be present in non-local measurements¹⁸. We use a lock-in technique to determine the linear V_1 and second-order V_2 components of the resulting root-mean-square signal. From them we extract the non-local resistances R_i contributing to the total signal $V = R_1 I + R_2 I^2$. All measurements are at room temperature, unless otherwise noted.

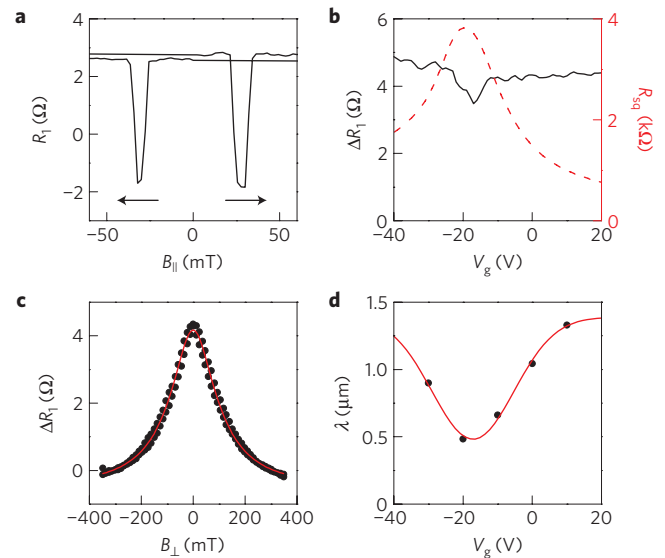


Figure 3 | Linear spin detection using a magnetic detector. **a**, Spin-valve effect in non-local linear resistance R_1 by sweeping an in-plane magnetic field at $V_g = 0$ V. Two well-defined values correspond to parallel (R_1^{Pa}) and antiparallel (R_1^{Ap}) alignment of Co contacts. **b**, Spin resistance $\Delta R_1 = R_1^{\text{Pa}} - R_1^{\text{Ap}}$ versus V_g . The dashed line is the square resistance R_{sq} of graphene between contacts 2 and 3 with $V_D \approx -20$ V. **c**, Hanle spin-precession curve by sweeping a perpendicular magnetic field at $V_g = 10$ V. The solid line is a fit with the one-dimensional Bloch equation. The obtained parameters are $D = 0.025$ m² s⁻¹ and $\tau = 71$ ps, with contact spin polarization $P = 9\%$. **d**, Spin-relaxation length $\lambda = \sqrt{D\tau}$, with D and τ extracted from Hanle curves taken at several values of V_g . The solid line is a fit with a Gaussian function for parameterization purposes.

We start by characterizing spin transport in the linear regime. The results in Fig. 3 show a non-local spin-valve effect, demonstrating spin transport between contacts 2 and 3, for a centre-to-centre separation of $L = 1.0$ μm and width of graphene $w \approx 1.1$ μm . The obtained spin resistance $\Delta R_1 \approx 4$ Ω is nearly constant versus the gate voltage V_g applied to the substrate. V_g controls the charge-carrier density n_g in graphene as $n_g = \gamma(V_g - V_D)$, with V_D the condition for charge neutrality (Dirac point) and $\gamma = 7.2 \times 10^{14}$ m⁻² V⁻¹. On the other hand, the graphene square resistance R_{sq} depends on V_g , changing by a factor of five. The observed ΔR_1 versus R_{sq} behaviour can be understood by the standard relation¹⁵ $\Delta R_1 = (P^2 R_{\text{sq}} \lambda / w) \exp(-L/\lambda)$, with P the spin polarization of the magnetic contacts, as being due to the charge-carrier-density dependence of λ with a minimum at the Dirac point. The latter is given by the behaviour of the spin-diffusion constant D and spin-relaxation time τ in graphene¹⁹⁻²¹ (Supplementary Section SA). Furthermore, the previous relation is valid only for contact resistances $R_c \gg R_{\text{sq}} \lambda / w$, where the contacts do not affect the spin transport^{16,17,22}. We take into account both considerations in our modelling below, by parameterizing λ (Fig. 3d) and by including the finite resistance of the contacts used for spin injection and detection.

Next, we demonstrate nonlinear detection of spins by using non-magnetic contacts. In Fig. 4b is shown a clear spin-valve effect in the second-order component V_2 of the non-local signal. The transitions in V_2 occur at the switching fields of the magnetic contacts used for current injection. We observe at zero gate voltage that $V_2^{\text{Ap}} > V_2^{\text{Pa}}$, consistent with the presence of a larger $\Delta\mu$ for the antiparallel magnetic configuration¹⁵ and a positive sign of the parameter α for electron transport¹². Therefore, we expect that the sign of the nonlinear spin resistance ΔR_2 should follow that of α and change sign when going from transport in the electron ($V_g > V_D$) to the hole ($V_g < V_D$) regime. The latter is

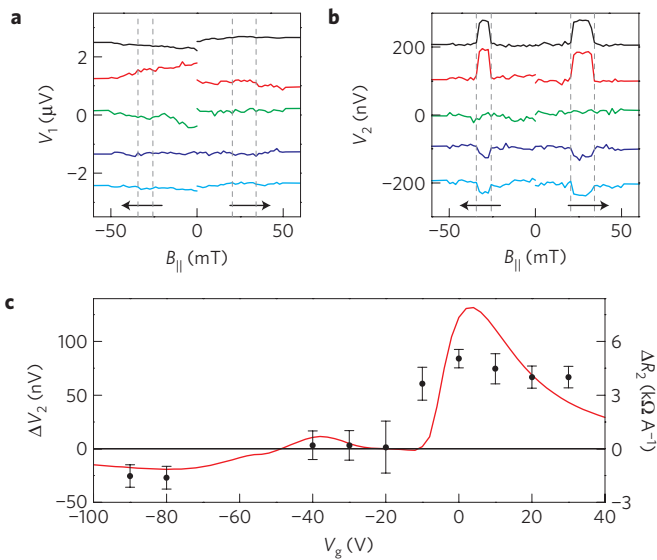


Figure 4 | Nonlinear spin detection using non-magnetic detectors. **a**, Linear non-local signal versus in-plane magnetic field; no spin-valve effect is observed. **b**, Second-order signal (same measurement as in **a**) showing spin-valve effect. Two well-defined values correspond to parallel (V_2^{Pa}) and antiparallel (V_2^{Ap}) alignment of the Co contacts. Curves in **a** and **b** correspond to (from top to bottom) $V_g = 30, 0, -40, -80$ and -90 V and are offset vertically for clarity. Each curve is the average of ten measurements. All data are for a root-mean-square current of $5 \mu\text{A}$ (configuration as in Fig. 2c). **c**, Nonlinear spin resistance $\Delta R_2 = R_2^{\text{Ap}} - R_2^{\text{Pa}}$ versus V_g . For each data point the average value of V_2 for (anti)parallel configuration, and its standard deviation, was extracted from curves such as those shown in **b**. The solid line is a result from numerical modelling.

confirmed by observing that $\Delta R_2 < 0$ for gate voltages $V_g \ll V_D$. We remark that the measured spin-valve signal cannot be explained by spurious detection of potentials in the current-carrying part of the sample, owing to the absence of spin-valve signal in the first-order response (Fig. 4a).

The gate-voltage dependence of the nonlinear spin resistance is presented in Fig. 4c. The ΔR_2 versus V_g curve shows a maximum of $\approx 5 \text{ k}\Omega \text{ A}^{-1}$ for electron transport. We did not observe a clear sign change when crossing the Dirac point, whereas for hole transport there was a minimum value of only $\approx -2 \text{ k}\Omega \text{ A}^{-1}$. To understand this electron-hole asymmetry we looked into the charge-transport properties of the detector circuit, between contacts 4 and 5. The Dirac curve in Fig. 5a shows that, while there is a reasonable symmetry for V_g close to $V_D = -9$ V, this is not the case for larger V_g , as shown by the kink visible at $V_g = -55$ V. Such kinks in the Dirac curve have been described as arising owing to electron doping from metal contacts with a thin oxide layer that prevents charge-density pinning²³. Our contacts are deposited onto a thin oxide barrier. Therefore, we interpret the Dirac curve of the detector circuit as being composed of two contributions, the graphene under (and next to) the contacts and that away from the contacts (curves 1 and 2 in Fig. 5a, Supplementary Section SB).

Having described both spin and charge transport in the linear regime, we now construct a minimal one-dimensional model that enables quantitative comparison with experiment. As mentioned above, we model $\Delta\mu$ by considering the induced conductivity spin polarization β , finite-resistance contacts and gate-voltage dependence of λ . We use a fixed $P = 9\%$ for the magnetic contacts (extracted in the regime $R_c \geq 5R_{\text{sq}}\lambda/w$) and a width profile for graphene as extracted from atomic force microscopy. Furthermore, we describe the Dirac curve for each graphene region using the approximate relation²⁴ $\sigma = v e(n_e^2 + n_h^2)^{1/2}$, with v the

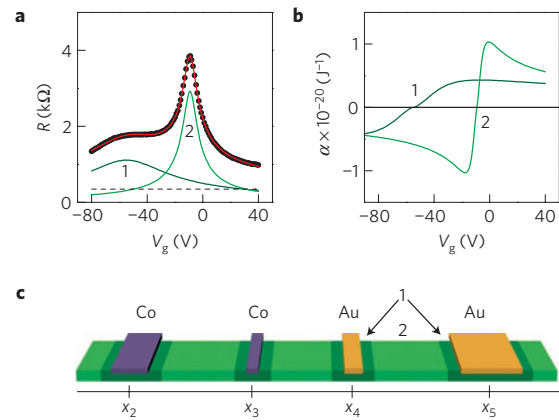


Figure 5 | Role of charge-density distribution. **a**, Resistance of graphene between contacts 4 and 5 (Au detectors). The red solid line is a fit using a phenomenological description including two Dirac curves (solid lines labelled 1 and 2) and a constant $0.35 \text{ k}\Omega$ for the low-resistance contact 5 (dashed line). **b**, Extracted parameter $\alpha = \sigma^{-1} \partial\sigma / \partial\epsilon$ for each of the two Dirac curves mentioned in **a**. **c**, Schematic representation of charge-density distribution within graphene. Different properties are considered for graphene under and next to the contacts (1) and for the region away from the contacts (2).

carrier mobility and n_i a background carrier density due to the presence of electron-hole puddles and thermally generated carriers. We then extract the parameter α for each region¹² (Fig. 5b) in a similar way to the extraction of the Seebeck coefficient of graphene from the Dirac curve^{14,24}.

The model, schematically shown in Fig. 5c, has the extension of the graphene region 1 beyond the contact edge as the only free parameter. Scanning photocurrent work²⁵ has shown that the doping in graphene decays gradually from the contact edge, extending up to a distance of $\approx 0.3 \mu\text{m}$. For simplicity we consider a constant doping up to a distance of $0.15 \mu\text{m}$. The modelled ΔR_2 -versus- V_g curve (solid line in Fig. 4c) successfully reproduces both the trend and the magnitude of the data. The agreement imparts certainty to our interpretation of the measured ΔR_2 signal as arising owing to the nonlinear interaction between spin and charge.

The magnitude of ΔR_2 is only slightly limited by the finite resistance of our contacts ($R_c \approx 7 \text{ k}\Omega$). Assuming infinite contact resistance, we predict only up to a twofold increase in ΔR_2 . On the other hand, the use of high-quality tunnel contacts²² with $P = 30\%$ would yield a tenfold increase. Moreover, as $\alpha_{\text{max}} \propto 1/\sqrt{n_i}$, similar to the Seebeck coefficient¹⁴, decreasing n_i by two orders of magnitude by using a boron nitride substrate²⁶ would yield a further tenfold increase. Therefore, the herewith demonstrated effect is a real candidate for spin detection. It can be regarded as a step in the logical progression from linear interactions between spin and charge towards interactions between spin and heat, as studied in the field of spin caloritronics²⁷.

Methods

Sample preparation. Graphene is obtained from highly oriented pyrolytic graphite by mechanical exfoliation and deposited on a highly n-doped Si substrate covered with a thermal oxide layer 300 nm thick. The Si substrate is used as electrostatic gate. Graphene is first covered by 0.8 nm Al followed by natural oxidation to obtain a thin aluminium oxide layer. Electron-beam lithography, deposition by evaporation and lift-off were carried out twice, first for the Ti/Au contacts and then for Co. We observed in previous samples a lower resistance of the Ti/Au contacts, which prevented us from using them for spin detection¹⁶. This problem was possibly related to the required baking of poly(methyl methacrylate) for the second electron-beam lithography step, which may cause diffusion of Ti/Au through the oxide barrier. To solve it we increased the thickness of the oxide barrier only for the Ti/Au contacts by deposition and oxidation of an extra 0.3 nm of Al. This yielded non-invasive Au contacts with similarly high resistances to those of the Co contacts.

Measurements. Characterization took place at room temperature and at 77 K (Supplementary Section SA) in a cryostat with a base pressure $\approx 1 \times 10^{-7}$ mbar. The sample was first annealed under vacuum at 130 °C for ≈ 24 h for removal of physisorbed water, resulting in low hysteresis in the Dirac curve ($\Delta V_D < 10$ V). This hysteresis leads to the increased uncertainty of ΔV_2 around $V_g = -20$ V seen in Fig. 4c. Measurements were made using a 1–5 μ A a.c. current source and recording simultaneously the first- and second-harmonic responses using two lock-in systems. All current and voltage signals reported are root-mean-square values. Therefore, the resistances were extracted as $R_1 = V_1/I$ and $R_2 = \sqrt{2}V_2/I^2$. Excitation frequency was kept at ≤ 3 Hz to prevent signals due to capacitive coupling, as determined by frequency scans. Contribution from higher harmonics was found to be negligible.

Modelling. We developed a one-dimensional finite-element code using the program MATLAB to find numerical solutions for the two-channel spin diffusion equations¹³

$$\frac{I_{\pm}}{w} = \sigma_{\pm} \frac{\partial \mu_{\pm}}{\partial x}$$

$$\frac{\partial^2 \Delta \mu}{\partial x^2} = \frac{\Delta \mu}{\lambda^2}$$

with the inclusion of an element-specific conductivity spin polarization¹² β , as described in the main text. Element length was kept ≤ 10 nm. I_{\pm} and $\Delta \mu$ were set to be continuous across element boundaries. We consider point contacts located at the centre of the fabricated electrodes, which could either inject a spin current PI or detect the electrochemical potential $\mu_{\text{avg}} + P\Delta\mu$. Spin relaxation under contacts with finite resistance (4.9, 9.2, 7.3 and < 1 k Ω for contacts 2, 3, 4 and 5, respectively) was implemented as in ref. 17, with the extra consideration of contact spin polarization P . We use a phenomenological description of each Dirac curve by the relation $\sigma = v e (n_g^2 + n_i^2)^{1/2}$, which describes the data using a constant mobility v by including the effect of electron-hole puddles through a background carrier density n_i (ref. 24). For each Dirac curve the parameter $\alpha = \sigma^{-1} \partial \sigma / \partial \epsilon$ is extracted using $\partial \sigma / \partial \epsilon = (\partial \sigma / \partial n_g) (\partial n_g / \partial \epsilon)$, in a manner similar¹² to that used in the literature for the Seebeck coefficient^{14,24}. The extracted parameters for the curve Dirac 2 (graphene between contacts) were $v = 3,900 \text{ cm}^2 \text{ V}^{-1} \text{ s}^{-1}$ and $n_i = 3.5 \times 10^{15} \text{ m}^{-2}$, consistent with previous experiments on SiO₂ substrates²⁴, whereas for Dirac 1 we obtained $v = 800 \text{ cm}^2 \text{ V}^{-1} \text{ s}^{-1}$ and $n_i = 2 \times 10^{16} \text{ m}^{-2}$. To obtain ΔR_2 we calculated the difference in potential $V = -\mu_{\text{avg}}/e$ between the Au detectors, for both parallel and antiparallel configurations and d.c. currents $I = \pm 5 \mu\text{A}$. The result was then fitted with $\Delta V = \Delta R_1 I + \Delta R_2 I^2$. The odd contribution $|\Delta R_1| < 3 \text{ m}\Omega$ was found to be negligible.

Received 27 September 2011; accepted 6 January 2012;
published online 12 February 2012

References

- Zutić, I., Fabian, J. & Das Sarma, S. Spintronics: Fundamentals and applications. *Rev. Mod. Phys.* **76**, 323–410 (2004).
- Chappert, C., Fert, A. & Van Dau, F. N. The emergence of spin electronics in data storage. *Nature Mater.* **6**, 813–823 (2007).
- Jedema, F. J., Filip, A. T. & van Wees, B. J. Electrical spin injection and accumulation at room temperature in an all-metal mesoscopic spin valve. *Nature* **410**, 345–348 (2001).
- Lou, X. *et al.* Electrical detection of spin transport in lateral ferromagnet–semiconductor devices. *Nature Phys.* **3**, 197–202 (2007).
- Valenzuela, S. O. & Tinkham, M. Direct electronic measurement of the spin Hall effect. *Nature* **442**, 176–179 (2006).
- Uchida, K. *et al.* Observation of the spin Seebeck effect. *Nature* **455**, 778–781 (2008).
- Abanin, D. A. *et al.* Giant nonlocality near the Dirac point in graphene. *Science* **332**, 328–330 (2011).

- Slachter, A., Bakker, F. L., Adam, J. & van Wees, B. J. Thermally driven spin injection from a ferromagnet into a non-magnetic metal. *Nature Phys.* **6**, 879–882 (2010).
- Le Breton, J., Sharma, S., Saito, H., Yuasa, S. & Jansen, R. Thermal spin current from a ferromagnet to silicon by Seebeck spin tunnelling. *Nature* **475**, 82–85 (2011).
- Cutler, M. & Mott, N. F. Observation of Anderson localization in an electron gas. *Phys. Rev.* **181**, 1336–1340 (1969).
- Castro Neto, A. H., Guinea, F., Peres, N. M. R., Novoselov, K. S. & Geim, A. K. The electronic properties of graphene. *Rev. Mod. Phys.* **81**, 109–162 (2009).
- Vera-Marun, I. J., Ranjan, V. & van Wees, B. J. Nonlinear interaction of spin and charge currents in graphene. *Phys. Rev. B* **84**, 241408(R) (2011).
- Valet, T. & Fert, A. Theory of the perpendicular magnetoresistance in magnetic multilayers. *Phys. Rev. B* **48**, 7099–7113 (1993).
- Zuev, Y. M., Chang, W. & Kim, P. Thermoelectric and magnetothermoelectric transport measurements of graphene. *Phys. Rev. Lett.* **102**, 096807 (2009).
- Tombros, N., Jozsa, C., Popinciuc, M., Jonkman, H. T. & van Wees, B. J. Electronic spin transport and spin precession in single graphene layers at room temperature. *Nature* **448**, 571–574 (2007).
- Schmidt, G., Ferrand, D., Molenkamp, L. W., Filip, A. T. & van Wees, B. J. Fundamental obstacle for electrical spin injection from a ferromagnetic metal into a diffusive semiconductor. *Phys. Rev. B* **62**, R4790–R4793 (2000).
- Popinciuc, M. *et al.* Electronic spin transport in graphene field-effect transistors. *Phys. Rev. B* **80**, 214427 (2009).
- Bakker, F. L., Slachter, A., Adam, J. & van Wees, B. J. Interplay of Peltier and Seebeck effects in nanoscale nonlocal spin valves. *Phys. Rev. Lett.* **105**, 136601 (2010).
- Józsa, C. *et al.* Linear scaling between momentum and spin scattering in graphene. *Phys. Rev. B* **80**, 241403(R) (2009).
- Avsar, A. *et al.* Toward wafer scale fabrication of graphene based spin valve devices. *Nano Lett.* **11**, 2363–2368 (2011).
- Han, W. & Kawakami, R. K. Spin relaxation in single-layer and bilayer graphene. *Phys. Rev. Lett.* **107**, 047207 (2011).
- Han, W. *et al.* Tunneling spin injection into single layer graphene. *Phys. Rev. Lett.* **105**, 167202 (2010).
- Nouchi, R. & Tanigaki, K. Charge-density depinning at metal contacts of graphene field-effect transistors. *Appl. Phys. Lett.* **96**, 253503 (2010).
- Grosse, K. L., Bae, M., Lian, F., Pop, E. & King, W. P. Nanoscale Joule heating, Peltier cooling and current crowding at graphene–metal contacts. *Nature Nanotech.* **6**, 287–290 (2011).
- Mueller, T., Xia, F., Freitag, M., Tsang, J. & Avouris, P. Role of contacts in graphene transistors: A scanning photocurrent study. *Phys. Rev. B* **79**, 245430 (2009).
- Xue, J. *et al.* Scanning tunnelling microscopy and spectroscopy of ultra-flat graphene on hexagonal boron nitride. *Nature Mater.* **10**, 282–285 (2011).
- Bauer, G. E., MacDonald, A. H. & Maekawa, S. Spin caloritronics. *Solid State Commun.* **150**, 459–460 (2010).

Acknowledgements

We would like to thank J. G. Holstein, B. Wolfs and M. de Roos for technical assistance. This work was financed by the Zernike Institute for Advanced Materials and by European Union Seventh Framework Programme Information and Communication Technologies grant no 257159 MACALO.

Author contributions

I.J.V.-M. and B.J.v.W. conceived and designed the experiments. I.J.V.-M. and V.R. carried out the experiments and data analysis. I.J.V.-M. wrote the paper, with contributions from the co-authors.

Additional information

The authors declare no competing financial interests. Supplementary information accompanies this paper on www.nature.com/naturephysics. Reprints and permissions information is available online at www.nature.com/reprints. Correspondence and requests for materials should be addressed to I.J.V.-M.